JGR Atmospheres

RESEARCH ARTICLE
10.1029/2023JD039776

Key Points:

- The regional precipitation extreme over Sichuan Basin (SCB) on 11–13 August 2020 cannot be reproduced without Tibetan Plateau (TP) or YGP
- The absence of TP (YGP) can reduce the accumulated precipitation regionally averaged over western SCB by 84% (51%)
- The absence of TP or YGP weakens the topographic lifting effect on airflow along the windward slope and reduces precipitation in western SCB

Correspondence to:
A. Huang and W. Zhao,
anhuang@nju.edu.cn;
zhaowei@nies.org

Citation:
Xu, X., Huang, A., Zhao, W., Yang, B., Xue, D., & Zhang, Y. (2024). Roles of the Tibetan Plateau and Yunnan-Guizhou Plateau in the regional extreme precipitation over Sichuan Basin in summer: A case study. *Journal of Geophysical Research: Atmospheres*, *129*, e2023JD039776. https://doi.org/10.1029/2023JD039776

Received 4 AUG 2023
Accepted 21 JAN 2024

Author Contributions:

Conceptualization: Anning Huang
Data curation: Xiaoke Xu, Daokai Xue, Yan Zhang
Formal analysis: Xiaoke Xu, Anning Huang, Wei Zhao, Ben Yang, Daokai Xue
Investigation: Xiaoke Xu, Anning Huang, Wei Zhao, Ben Yang, Daokai Xue
Methodology: Xiaoke Xu, Anning Huang
Resources: Xiaoke Xu, Daokai Xue, Yan Zhang
Software: Xiaoke Xu
Supervision: Wei Zhao
Validation: Xiaoke Xu, Anning Huang, Ben Yang
Visualization: Anning Huang
Writing – original draft: Xiaoke Xu
Writing – review & editing: Xiaoke Xu, Anning Huang, Wei Zhao, Ben Yang, Daokai Xue, Yan Zhang

Roles of the Tibetan Plateau and Yunnan-Guizhou Plateau in the Regional Extreme Precipitation Over Sichuan Basin in Summer: A Case Study

Xiaoke Xu[1], Anning Huang[1,2], Wei Zhao[3], Ben Yang[1], Daokai Xue[1], and Yan Zhang[4]

[1]School of Atmospheric Sciences, Nanjing University, Nanjing, China, [2]Qinghai Lake Comprehensive Observation Research Station, Chinese Academy of Sciences, Gangcha, China, [3]Nanjing Institute of Environmental Sciences, Ministry of Ecology and Environment of the People's Republic of China, Nanjing, China, [4]Key Laboratory of Radiometric Calibration and Validation for Environmental Satellites, National Satellite Meteorological Center, China Meteorological Administration (LRCVES/CMA), FengYun Meteorological Satellite Innovation Center (FY-MSIC), Beijing, China

Abstract The roles of the Tibetan Plateau (TP) and Yunnan-Guizhou Plateau (YGP) in regional precipitation extremes over the Sichuan Basin (SCB) in summer under specific circulation background remain unclear. This study quantifies the impact of TP or YGP on the regional extreme precipitation event (REPE) which occurred during 04:00 Beijing time (BJT) on 11 August to 03:00 BJT on 13 August 2020 with a rainfall center located in the western SCB based on numerical experiments. Results show that the accumulated precipitation regionally averaged over the western SCB during the REPE can be reduced by 84% (51%) when the TP (YGP) is absent, and the decreased precipitation is mainly caused by the reduced stratus precipitation. Mechanism analysis indicates that relative to the control experiment including the TP and YGP, the absence of TP or YGP leads to reduced temperature over the SCB induced by anomalous cold advection from the upstream regions where the terrains are removed, and further results in much more stable stratification and thereafter weakens the ascending motions and reduces the stratus precipitation over the western SCB. On the other hand, the absence of TP or YGP induces an anomalous anti-cyclone at 850 hPa over SCB, which further weakens both the uplift effect of terrain on airflow along the windward slope and water vapor transport over the western SCB and thereafter reduces the precipitation over this region. This study deepens the understanding of the topographic effect on regional extreme precipitation over SCB in summer from the thermodynamic and dynamic processes.

Plain Language Summary Tibetan Plateau (TP) and Yunnan-Guizhou Plateau (YGP) play important roles in the formation of summer regional extreme precipitation event (REPE) over Sichuan Basin (SCB) under specific circulation background. This study addresses how the TP or YGP affects the REPE over SCB during 04:00 Beijing time (BJT) on 11 August to 03:00 BJT on 13 August 2020 based on numerical experiments. Results show the absence of TP (YGP) can reduce the accumulated precipitation during the REPE regionally averaged over the western SCB by 84% (51%). The absence of TP or YGP leads to reduced temperature over SCB induced by anomalous cold advection from the upstream regions where the terrains are removed and much more stable stratification, and thereafter weakens the large-scale ascending motions and reduces the stratus precipitation over western SCB. Meanwhile, an anomalous anti-cyclone at 850 hPa over the SCB is induced by the absence of TP or YGP. This can further weaken the uplift effect of terrain on airflow along the windward slope and water vapor transport over western SCB and result in decreased accumulated precipitation over this region. Findings of this study can provide a base for the refined simulation and prediction of REPE over regions with complex terrain.

1. Introduction

Sichuan Basin (SCB) is located in southwestern China, and is surrounded by the Tibetan Plateau (TP), the Yunnan-Guizhou Plateau (YGP), Southeast Hills, and Daba Mountains (Bin & Xiang, 2016; Du et al., 2022; J. Li et al., 2021). Affected by terrain, the precipitation (including extreme precipitation with different duration) over the SCB exhibits a significant diurnal feature (M. G. Wu & Luo, 2019; Zheng et al., 2019), which usually begins at night, peaks between midnight and early morning, and gradually ceases after sunrise (S. Chen et al., 2019; J. Liu et al., 2021; Y. Wu et al., 2018; Zhao et al., 2020; L. Zhu et al., 2018). In recent years, the frequency/intensity

of extreme precipitation (especially hourly extreme precipitation) has considerably increased over the SCB (Deng et al., 2022; Han et al., 2019; Lei et al., 2022; L. Li et al., 2020; X. Li et al., 2022; Park & Min, 2017). Previous studies show that the extreme precipitation over the SCB is shaped by the complex terrain (Hu et al., 2021; C. H. Huang et al., 2022; Nie & Sun, 2021; Y. Zhang et al., 2021).

Topography greatly affects the synoptic-scale systems, such as the location of South Asia High (SAH), the position of North Pacific Subtropical High (WNPSH), and the formation and intensity of Southwest Vortex (SWV), which control the precipitation extremes over the SCB in summer (J. Li et al., 2021; Q. R. Ma et al., 2022; Ng et al., 2021; Qiao et al., 2022; A. Wu & Li, 2022; Xia et al., 2021; X. Xu et al., 2023; Y. Zhang et al., 2021). The TP acting as the heat source in summer favors the development and maintenance of SAH (Y. Fu et al., 2020; Y. Liu et al., 2020; G. Wu et al., 2015). The WNPSH is blocked by the TP and controls the water vapor transport of SCB (H. Xu et al., 2020; Q. Zhang et al., 2017). The branches of the westerly flow and the eastward-propagating plateau trough converge over the SCB and result in the SWV (S. M. Fu et al., 2019; Q. R. Ma et al., 2022; Q. W. Wang & Tan, 2014; Z. Wu et al., 2022). In addition, the complex terrain crucially influences the convective systems in the aspects of the convective initiation and the uplifting, drag, and blocking of the flow (X. Huang et al., 2020; Jin et al., 2013; Q. R. Ma et al., 2022; Y. Wang et al., 2020; Y. Zhang et al., 2019).

The role of the topography in the formation of extreme precipitation over the SCB is complicated (Hua et al., 2020; Wan et al., 2017; Z. Wu et al., 2022; Xia et al., 2021). During the daytime, the surface heat difference between the plateau and basin results in the mountain–plains solenoid and promotes the initiation of the middle-scale convective system (MCS) (Bao et al., 2011; Jin et al., 2013; Sun & Zhang, 2012; W. Xu & Zipser, 2011). During the nighttime, the topographic gravity waves generate the unstable layer and strengthen the MCS propagated from the upper reaches (Hua et al., 2020). Meanwhile, topography slows down the movement of MCS and thus lengthens the duration of precipitation (C. H. Huang et al., 2022; Kang et al., 2019; Phadtare, 2018). The enhancement of the boundary layer southwest low-level jet (LLJ) provides abundant water vapor at night, this is closely related to the complex terrain (Qiao et al., 2022; Shen et al., 2022). However, the physical processes of the terrain effects on the formation and enhancement of extreme precipitation over the SCB are not well revealed.

To solve this puzzle, a series of numerical simulations have been carried out by decreasing altitude, smoothing terrain, or turning off the thermodynamic process (Almazroui et al., 2018; Cannon et al., 2017; Nielsen et al., 2016; Wan et al., 2017; H. Xu & Yao, 2015; K. Yang et al., 2022; Zhao, 2012). Some of them believe that the dynamic effects of the TP or YGP dominate the extreme precipitation over the SCB (J. Chen et al., 2007; Formetta et al., 2022; Hu et al., 2021; Son et al., 2020). For instance, the westerly winds blocked by the TP are the primary cause of the SWV formation (Q. R. Ma et al., 2022; Z. Wu et al., 2022; Y. Zhang et al., 2021). The TP can make the MCS maintain over the SCB for a long time and result in extreme precipitation (C. H. Huang et al., 2022; Z. Wu et al., 2022). Some others agree that the thermodynamic effects of TP and YGP to control the extreme precipitation over the SCB (Wan et al., 2017; Q. Wang et al., 2016; K. Yang et al., 2022). The diurnal variation of surface heat flux between the plateaus (TP and YGP) and SCB reinforces the convective instability over the SCB and favors the initiation of MCS (Jin et al., 2013; Sun & Zhang, 2012; Z. Wu et al., 2022). The difference in the surface heat flux between the plateau and basin enhances the atmospheric baroclinicity, resulting in stronger LLJ than those over the flat areas (He & Zhang, 2010; Xia et al., 2021; Y. Zhang et al., 2019; Zhao, 2012). On the contrary, Nielsen et al. (2016) claim that the topographic steepness has no impact on the extreme precipitation. In general, the primary impacts of the terrain on the extreme precipitation over the SCB are still controversial and worthy to be investigated systematically and quantitatively (Luo et al., 2016; Roe, 2005; M. G. Wu & Luo, 2019; Zheng et al., 2019).

A persistent rainfall event occurred in the SCB during 10–18 August 2020, it broke the record since 1960 in average 24 hr precipitation over southwestern China (Hu et al., 2021; Q. R. Ma et al., 2022; Qian et al., 2022). The max precipitation intensity and amount mainly concentrate on 11–13 August 2020 and 16–18 August 2020 (Q. R. Ma et al., 2022). Among them, the period of 11–13 August 2020 matches the definition of the regional extreme precipitation event (REPE) detected by X. Xu et al. (2023). Previous studies on this event mainly focus on the diagnostic analysis of convective systems, but there is a shortage of quantitative investigation on the impact of special terrain in regional extreme precipitation over SCB (Qian et al., 2022; Xia et al., 2021; J. Zhang & Sun, 2021). Therefore, we chose the typical long-duration REPE during 04:00 Beijing time (BJT) on 11 August to 03:00 BJT on 13 August 2020 to investigate the topographic effect of this REPE based on numerical experiments. Here we attempt to address two questions: (a) How does the large-scale terrain of TP or YGP affect the REPE?

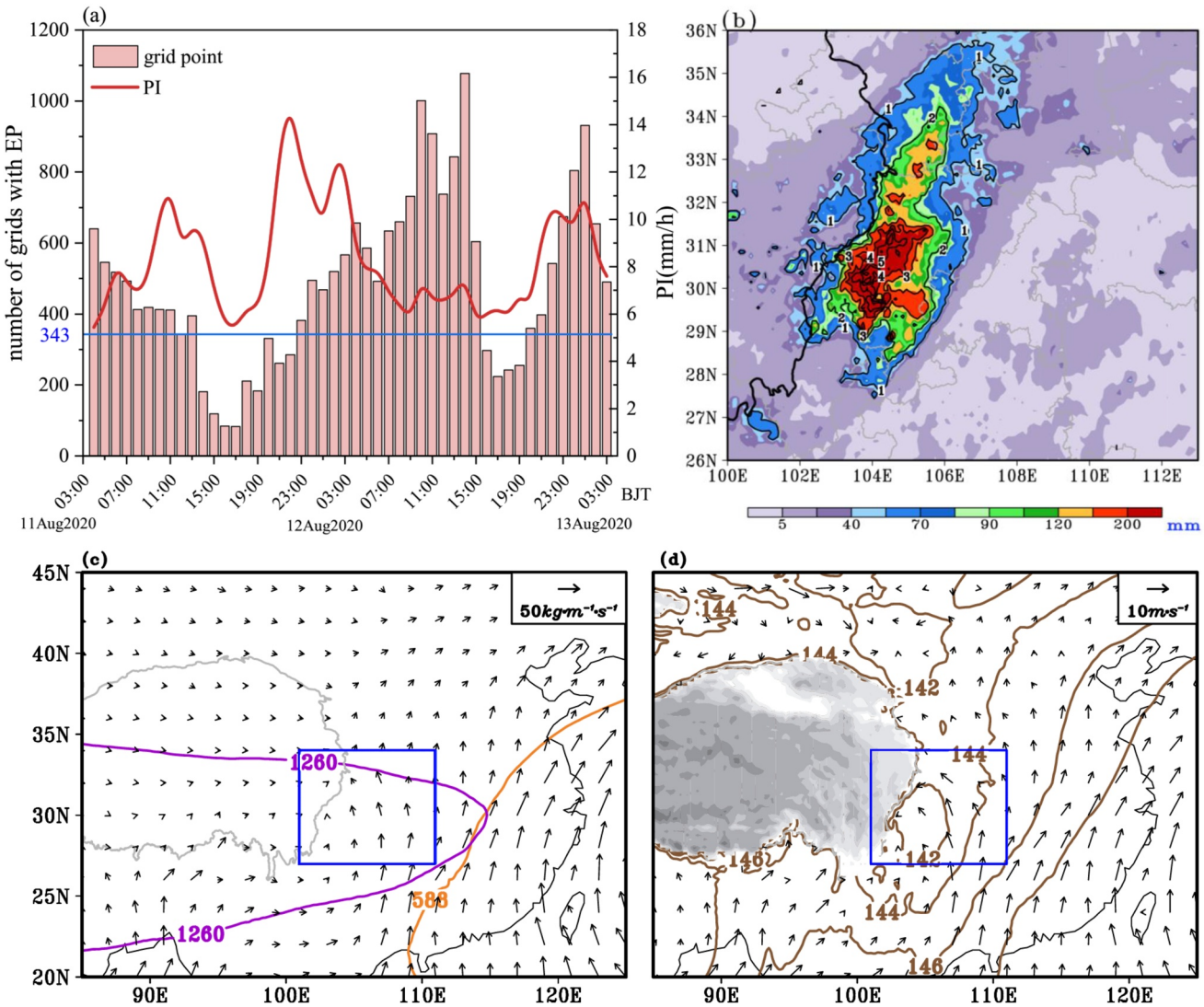

Figure 1. (a) Temporal variation of mean hourly precipitation over the grids with simultaneous extreme precipitation (red line, unit: mm·h^{-1}) and the temporal variation of grid numbers with EP simultaneously (pink bar, unit: grid point) over the region of 102°–108°E, 29°–33°N during the 04:00 (BJT) on 11 August-03:00 (BJT) on 13 August 2020. The blue line symbolizes the regional extreme precipitation threshold of grid numbers according to X. Xu et al. (2023). (b) Spatial distribution of the mean accumulated total precipitation (shade, unit: mm) and precipitation intensity (contour, unit: mm·h^{-1}) from GPM data during this regional extreme precipitation event. (c) Atmospheric circulation in middle and upper layers including South Asia High (purple line), WNPSH (orange line), and vertically integrated water vapor flux (vector, unit: kg·m^{-1} s^{-1}). The blue rectangular in (c) represents the Sichuan Basin. (d) Atmospheric circulation on 850 hPa including the geopotential height (contour, unit: dagpm), wind field (vector, unit: m·s^{-1}), and terrain height over 2,500 m are shown by gray shadings.

(b)What are the underlying physical mechanisms from the perspective of dynamical and thermal processes? The findings of this study could deepen the understanding of mechanisms in complex topography affecting extreme precipitation.

2. Background, Data, Numerical Design, and Methodology

2.1. Background

According to the definition of REPE in X. Xu et al. (2023), the time of the grid points with simultaneous extreme precipitation in the SCB reached the grid threshold (197 grid points, the blue line in Figure 1a) of the REPE is 44 hr during the 48-hr persistent heavy rainfall event, which occurred between 04:00 BJT on 11 August and 03:00 BJT on 13 August 2020. As shown in Figure 1a, the precipitation intensity regionally averaged over the grids with simultaneous extreme precipitation in the SCB is over 5 mm·h^{-1} during 04:00

BJT on 11 August to 03:00 BJT on 13 August 2020. Although some hourly extreme precipitation at certain times does not reach the regional grid number threshold, we still treat it as an event to study the integrity of the precipitation process.

From Figure 1b, the accumulated rainfall center during the REPE is located in the western SCB next to the TP with the intensity more than 200 mm. As mentioned by X. Xu et al. (2023), the typical synoptic pattern responsible for this kind of REPE is featured by the westward-extended WNPSH at 500 hPa and eastward-extended SAH at 200 hPa (Figure 1c) with a low-level vortex over SCB at 850 hPa (Figure 1d). In this study, we focus on addressing how TP or YGP affects this kind of REPE in the SCB (27°–34°N, 101°–111°E) indicated by the blue rectangle in Figure 1c under a specific atmospheric circulation background.

2.2. Data

1. The half-hourly precipitation of Integrated Multi-satellite Retrievals for Global Precipitation Measurement (GPM-IMERG V06) with a resolution of 0.1° from 04:00 BJT on 11 August to 03:00 BJT on 13 August 2020 is used in this study (Hou et al., 2014), it can be available at https://disc.gsfc.nasa.gov/datasets/GPM_3IMERGDF_06/summary/. This data set can properly capture the time-spatial distribution and intensity of extreme precipitation events over the SCB (M. Yang et al., 2020).
2. The fifth ECWMF (ERA5) hourly reanalysis data with a horizontal resolution of 0.25° from 04:00 BJT on 11 August to 03:00 BJT on 13 August 2020 (Hersbach et al., 2020, https://cds.climate.copernicus.eu/cdsapp#!/search?type=dataset), are used to conduct model evaluation.
3. The National Centers for Environmental Prediction final (FNL) global analysis data (D. Huang & Gao, 2018) with 6 hourly time resolutions and 1° × 1° horizontal resolution (http://weather.uwyo.edu/upperair/sounding.html/) provide the initial and lateral boundary conditions for the WRF model (Cai et al., 2021; Mun et al., 2017).

2.3. Numerical Experimental Design

The version 4.2 of WRF model (Skamarock et al., 2019) is used in this study to investigate the impact of topography on the REPE over SCB. We set up two sensitive experiments named TP_N and YG_N and a control experiment (CTL). The CTL experiment used the default configuration containing the real orography of TP and YGP (Figure 2a). In the TP_N experiment, the TP over the area of 27°–40°N and 85°–104.5°E (Cui et al., 2021; Gu et al., 2020; Tang et al., 2018) was replaced by the flat ground with 500 m height, which is the same height as the mean altitude of SCB (Figure 2b). In the YG_N, the YGP over the area of 20°−28°N and 90°−107°E (Guo et al., 2022; Shi et al., 2017; D. Zhu et al., 2022) is set to a flat ground with 500 m height (Figure 2c).

Through a series of test experiments, it is found that the simulation results driven by NCEP with 12 hr spin-up time are similar to the ensemble simulation and better than those driven by the ERA5 data (not shown), thus the model initial/lateral boundary conditions in this study were directly derived from the NCEP data. All experiments adopt the same model configuration and initial/lateral boundary conditions (the 6-hourly reanalysis data from the NCEP) except for setting different model terrains. A two-way nest with a horizontal resolution of 18 km in the "mother" domain and 6 km in the nested domain (Figure 2d) with 41 vertical levels. The physical parameterization schemes are the same in the two nests. Each experiment starts at 00:00 (UTC) on 10 August 2020 and ends at 00:00 (UTC) on 13 August 2020 with the first 12 hr as the spin-up time (Chu et al., 2018; Y. Liu et al., 2023; Short & Petch, 2022; Ulmer & Balss, 2016). The lateral boundary and initial conditions for all experiments are derived by the same horizontal interpolation method called Smolarkiewicz (SINT) (Kuo et al., 1999) and linear interpolation is used in the terrain-following coordinate system (eta $= \frac{P - P_{top}}{P_s - P_{top}}$), which interpolated the FNL data onto the WRF model grids at each vertical layer. Following D. Huang and Gao (2018) and Cai et al. (2021), the physical parameterization schemes adopted in current study are listed as follows: the Morrison 2-moment microphysics scheme (Morrison et al., 2009), the Yonsei University planetary boundary layer scheme (Hong et al., 2006), the Grell–Freitas ensemble cumulus parameterization scheme (Grell & Freitas, 2014), the CAM shortwave and longwave radiation schemes (Collins et al., 2014), and the unified Noah land surface model (Tewari et al., 2004).

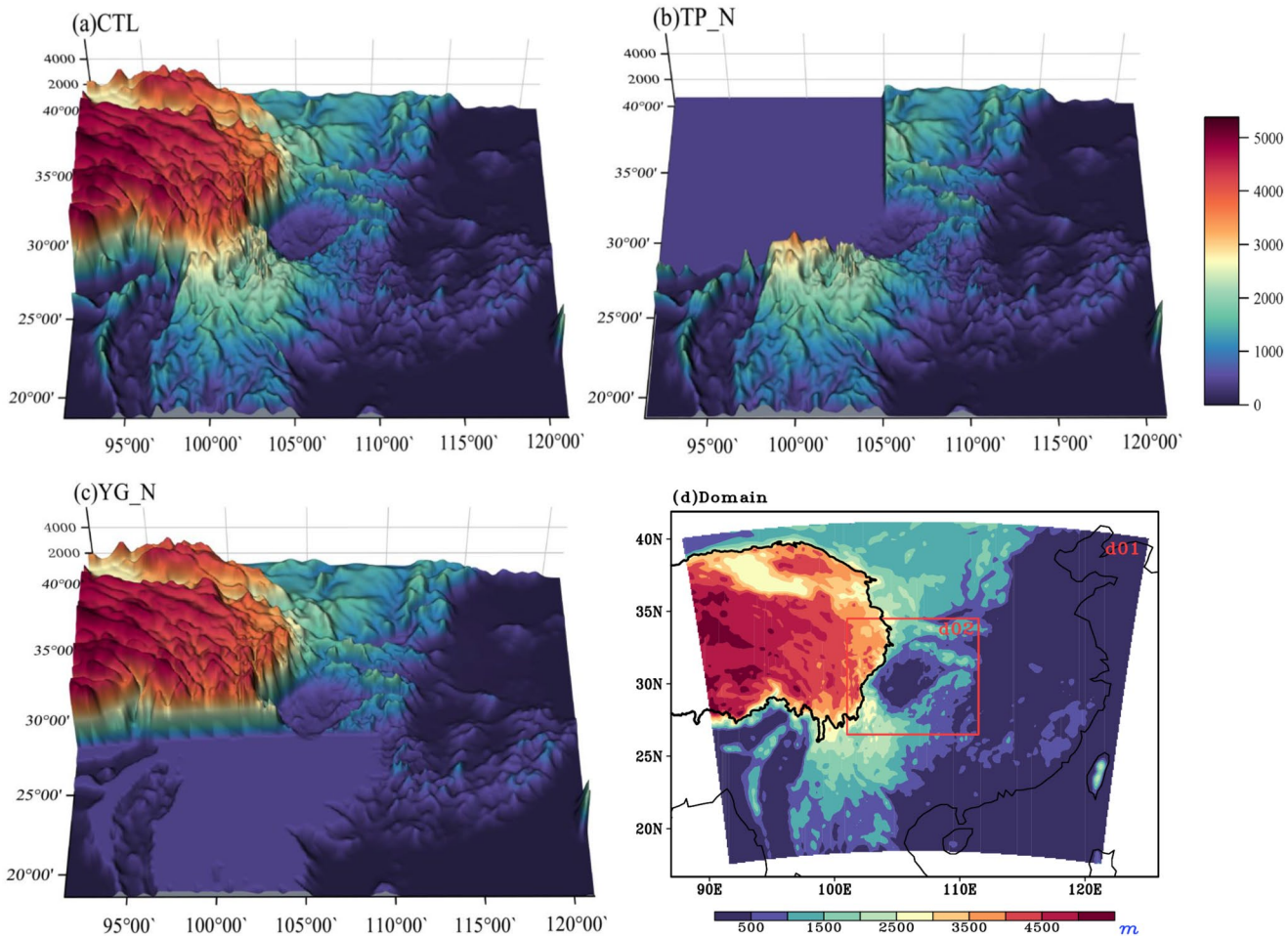

Figure 2. (a–c) Three-dimensional terrain distribution. Shading indicates the altitude. (a) Represents the real terrain in the CTL experiment, (b) is the TP_N sensitive experiment without Tibetan Plateau over the area of 27°–40°N, 85°–104.5°E, and (c) is the YG_N sensitive experiment without YGP over the area of 20°–28°N, 90°–107°E. (d) The nesting strategy, and domains used in WRF (unit: m).

2.4. Methodology

A water vapor budget analysis was conducted based on the moisture budget equation (P. Li et al., 2020; Lin et al., 2014; S. Ma & Zhou, 2015). The original equation used in this research is:

$$P = -\frac{\partial q}{\partial t} - \nabla \cdot \vec{V} q + E + \delta \tag{1}$$

Then

$$\nabla \cdot \vec{V} q = \frac{\partial qu}{\partial x} + \frac{\partial qv}{\partial y} + \frac{\partial qw}{\partial z} = \nabla_h \cdot \left(\vec{V}_h q\right) + \frac{\partial wq}{\partial z} \tag{2}$$

Under the p coordinate system:

$$P = -\frac{1}{g}\int_{P_s}^{P_t} \frac{\partial q}{\partial t} dp - \frac{1}{g}\int_{P_s}^{P_t} \nabla_h \left(q\overrightarrow{V_h}\right) dp - \frac{1}{g}\int_{P_s}^{P_t} \frac{\partial \omega q}{\partial p} dp + E + S \tag{3}$$

Where P denotes the precipitation rate, $-\frac{1}{g}\int_{P_s}^{P_t} \frac{\partial q}{\partial t} dp$ indicates the variation in local moisture with time, $-\frac{1}{g}\int_{P_s}^{P_t} \nabla_h \left(q\overrightarrow{V_h}\right) dp$ is the convergence of horizontal moisture flux and $\nabla_h = \frac{\partial}{\partial x} + \frac{\partial}{\partial y}$, $-\frac{1}{g}\int_{P_s}^{P_t} \frac{\partial \omega q}{\partial p} dp$ describes the vertical transport of moisture flux, E is the evaporation rate, and S is the residual term produced by the surface

process relative to topography and model bias. The $g, \omega, q, \vec{V_h}$ represents the acceleration of gravity, vertical velocity, specific humidity, and wind vector, respectively. P_t and P_s are the top and surface pressure, respectively.

$$-\frac{1}{g}\int_{P_s}^{P_t}\frac{\partial \omega q}{\partial p}dp = \frac{1}{g}\left[\int_{P_s}^{P_t}\overline{\omega}\frac{\partial q'}{\partial p} + \int_{P_s}^{P_t}\overline{q}\frac{\partial \omega'}{\partial p} + \int_{P_s}^{P_t}\frac{\partial \omega' q'}{\partial p}\right]dp \quad (4)$$

In addition, the vertical transport of moisture flux item in Equation 1 can be further decomposed into Equation 2. Among them, the $\int_{P_s}^{P_t}\overline{\omega}\frac{\partial q'}{\partial p}dp$ is associated with the changes in specific humidity induced by temperature changes, representing the thermodynamic process. The $\int_{P_s}^{P_t}\overline{q}\frac{\partial \omega'}{\partial p}dp$ is related to the vertical velocity induced by the variation of atmospheric circulation, indicating the dynamic process. The $\int_{P_s}^{P_t}\frac{\partial \omega' p'}{\partial p}dp$ denotes the nonlinear item associated with the product of changes in vertical velocity ω and water vapor q (S. Ma & Zhou, 2015; Seager et al., 2010).

The influence of the terrain on the REPE is illustrated by the differences between each sensitive experiment and the CTL experiment. The significance of differences is determined by the student's *t*-test (Lehmann, 1992; Student, 1908).

3. Results

3.1. Model Validation

Figure 3 provides the comparison of accumulated precipitation, mean precipitation intensity, and atmospheric circulation in the REPE during 04:00 BJT on 11 August 2020 to 03:00 BJT on 13 August 2020 from the observation and the CTL experiment simulation. It is clear that the WRF model can reasonably reproduce the spatial pattern of accumulated precipitation with a spatial correlation coefficient of 0.64, which is significant at 0.05 level. Due to the selected case in this study having continuous rain during the 48-hr period, the spatial distribution of precipitation intensity is the same as accumulated precipitation. Meanwhile, the spatial distribution of atmospheric circulation can be reasonably reproduced by the CTL experiment at difference levels (Figures 3c–3h), except that the slight bias in the location and intensity of SAH indicated by the 1,260 dagpm contour line at 200 hPa (G. Wu et al., 2015) (Figures 3c and 3d) and the marginal bias of WNPSH indicated by the 588 dagpm contour line at 500 hPa (Wei et al., 2014) relative to the ERA5 data (Figures 3e and 3f). The low-level vortex at 850 hPa simulated by the CTL experiment is closely identical to that in the ERA5 (Figures 3g and 3h). Overall, the WRF model can well reproduce the spatial distribution of rainfall over the SCB and atmospheric circulations at different levels during this REPE.

3.2. Impact of TP or YGP on the Accumulated Precipitation of the REPE

In the CTL experiment, the center of accumulated precipitation with the intensity more than 80 mm mainly distributes in the western SCB and along the east edge of TP (Figure 4a). However, the large rainfall center disappears when the TP (YGP) is absent in the TP_N (YG_N) experiment with scattered precipitation located in the northern SCB (Figures 4b and 4c). The rainfall differences between the TP_N experiment and CTL experiment show a large negative center located in the western SCB (Figure 4d) with the accumulated precipitation during the REPE regionally averaged over the area of 102°–108°E and 29°–33°N remarkably decreased from 77.25 mm in the CTL experiment to 11.5 mm in the TP_N experiment (Figure 4f), the absence of TP can lead to 84% reduction of the accumulated rainfall. Compared to the CTL experiment, the YG_N experiment without YGP also can diminish the accumulated precipitation in the western SCB (Figures 4c and 4e). From Figure 4f, the absence of YGP can lead to the accumulated rainfall during the REPE regionally averaged over the area of 102°–108°E and 29°–33°N decreased from 77.25 mm in the CTL experiment to 35.34 mm with the reduction of 51% relative to the CTL experiment (Figure 4f). Overall, both TP and YGP can obviously intensify the regional extreme rainfall in the western SCB except that the TP shows much stronger impact than the YGP.

To further reveal the source of the difference in the accumulated precipitation between the sensitive experiment and CTL experiment, the differences in the cumulus and stratus precipitation during the REPE are shown in Figure 5. Relative to the CTL experiment, the obviously reduced accumulated cumulus (stratus) precipitation due to the absence of TP in the TP_N experiment is mainly located over the western SCB and along the east edge of

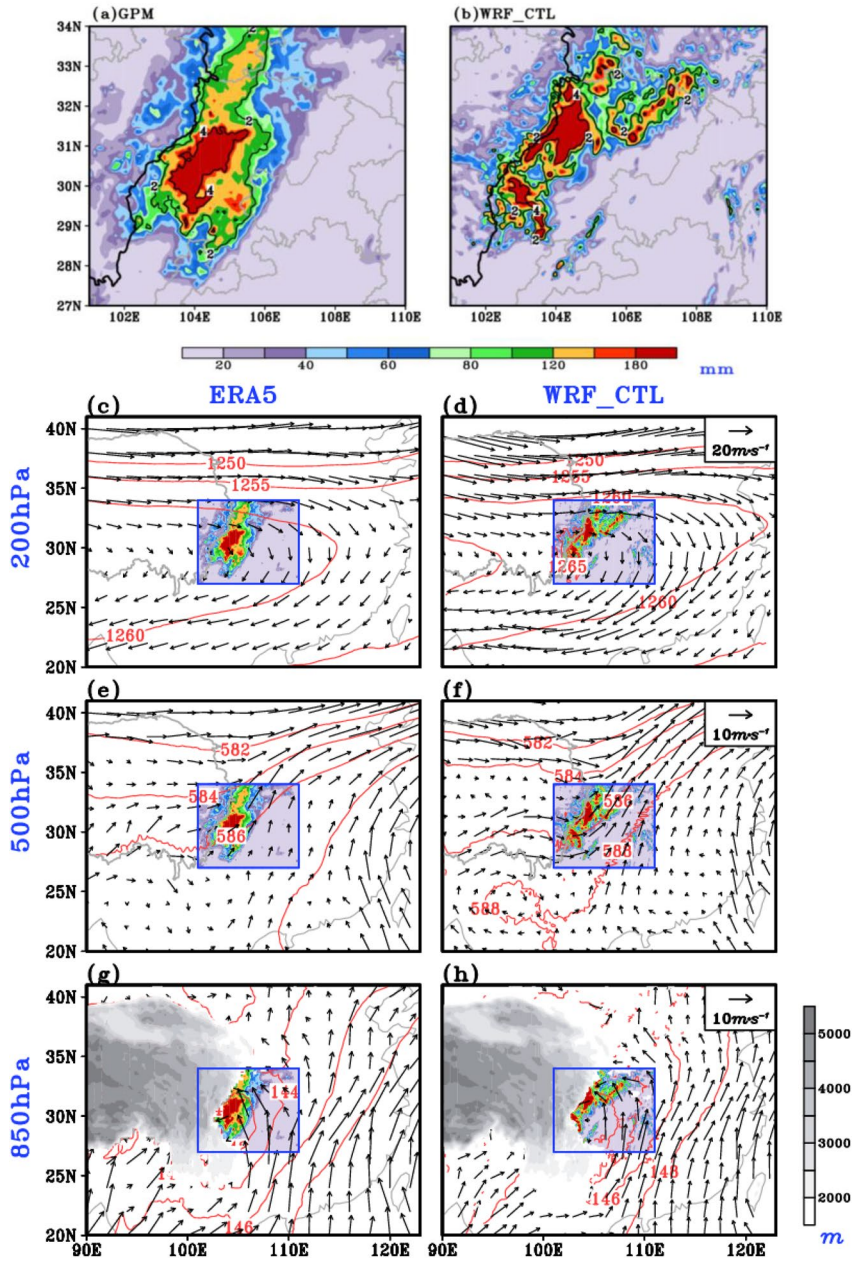

Figure 3. (a and b) Spatial distribution of mean accumulated precipitation (shade, unit: mm) and mean hourly precipitation (contour, unit: mm h^{-1}) from the GPM data and CTL modeled results during the 04:00 (BJT) on 11 August-03:00 (BJT) on 13 August 2020. (c–h) The spatial distribution of mean geopotential height (contour, unit: dagpm), wind (unit: $m{\cdot}s^{-1}$) at 200, 500, and 850 hPa, and accumulated precipitation (shaded, unit: mm) during this regional extreme precipitation event. The gray shaded represents the terrain. The blue rectangles indicated the location of Sichuan Basin.

TP (Figures 5a and 5d) with the reduction of 67% (86%) in the regional mean rainfall over the area of 102°–108°E and 29°–33°N (Figures 5c and 5f). Similar situations can be noted when the YGP is absent (Figures 5b–5f), despite that relative to the CTL experiment the reduction of 38.8% (53%) in the accumulated cumulus (stratus) precipitation regionally averaged over the area of 102°–108°E and 29°–33°N due to the absence of YGP is much weaker than that due to the absence of TP. It is worth noticing that the horizontal resolution in the inner nested domain is 6 km, which could explicit part of the deep convection. Even the calculated stratus precipitation may contain some deep convective precipitation. Stratus precipitation still dominates this REPE with verification and comparison by ERA5 data (not shown). In general, the absence of TP or YGP can lead to decreased stratus

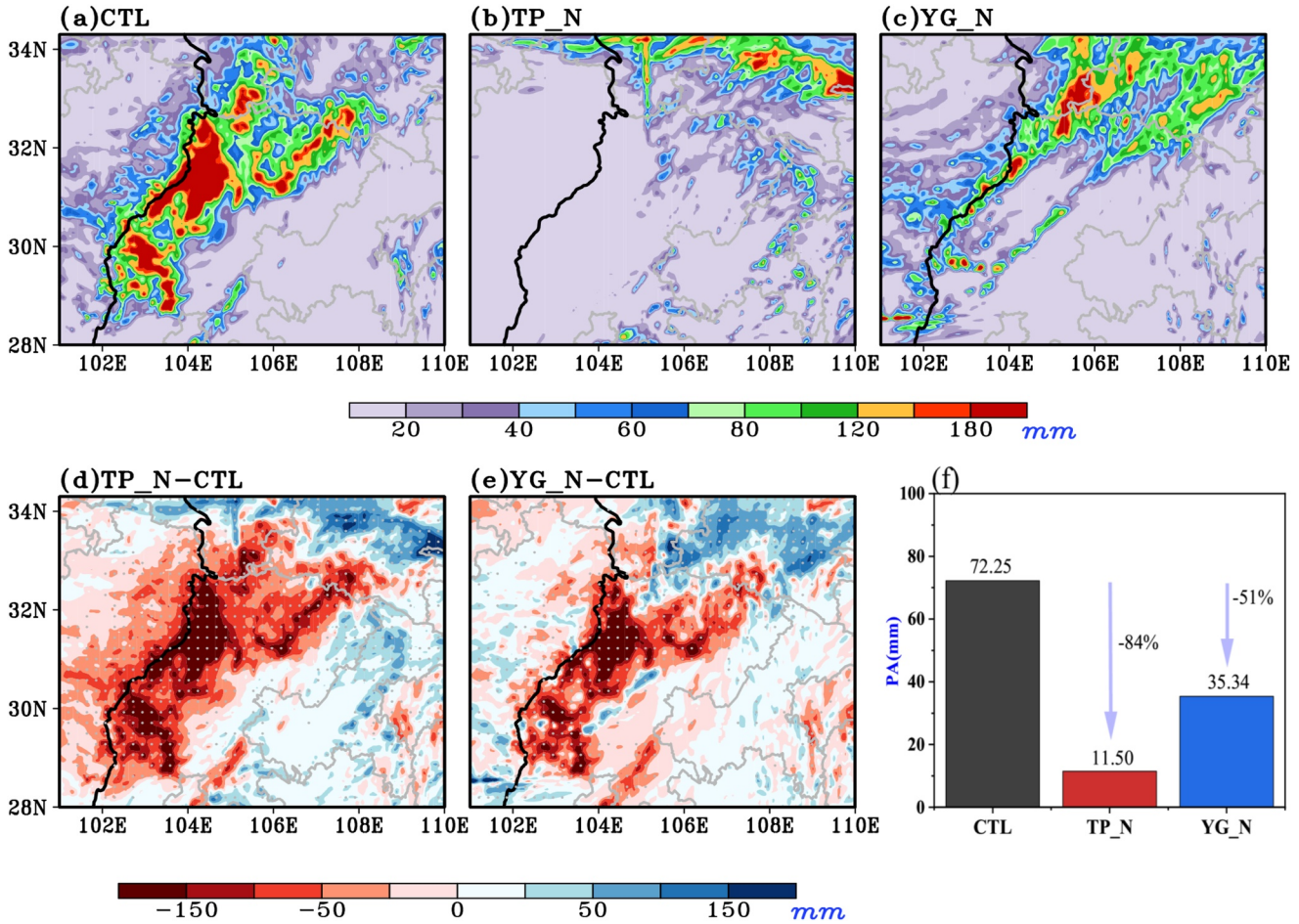

Figure 4. (a–c) The spatial distribution of accumulated precipitation (unit: mm) of each sensitive experiment and CTL experiment during 04:00 (BJT) on 11 August-03:00 (BJT) on 13 August 2020. (d–e) The difference of accumulated precipitation between each sensitive experiment and CTL experiment during this regional extreme precipitation event (REPE). The gray dots symbolize the significance above 95% of the *t*-test. (f) The histogram of accumulated precipitation (unit: mm) over the area of 102°–108°E and 29°–33°N during this REPE. The number at the top of the bar is a value of accumulated precipitation amount during the REPE regionally averaged over the area of 102°–108°E and 29°–33°N. The purple arrows and beside numbers represent the decreased value of rainfall amount relative to the CTL experiment.

and cumulus precipitation with much larger reduction in the stratus precipitation, which mainly results in the decrease of accumulated total precipitation.

4. Possible Mechanisms

4.1. Moisture Budget Diagnosis

In this section, we further reveal the physical mechanism based on the moisture budget diagnosis. Figure 6a shows the difference in each term of Equation 1 during the REPE regionally averaged over the area of 102°–108°E and 29°–33°N between each sensitive experiment and CTL experiment. P represents the hourly precipitation rate. It is clear that the mean hourly precipitation during the REPE regionally averaged over the area of 102°–106°E and 29°–33°N can be reduced by 1.55 mm·h^{-1} (0.9 mm·h^{-1}) due to the absence of TP (YGP). $-dqdt$ symbolizes the variation in local moisture with time and is associated with the atmospheric precipitable water. When the TP (YGP) is absent, the mean $-dqdt$ during the REPE regionally averaged over the area of 102°–106°E and 29°–33°N can be reduced by 0.32 mm·h^{-1} (0.013 mm·h^{-1}). The convergence item Conv(Vq) indicates the large-scale uplift movement over the region of 29°–33°N and 102°–108°E. Due to the absence of TP (YGP), the Conv(Vq) can be decreased by 1.44 mm·h^{-1} (0.78 mm·h^{-1}) in the TP_N (YG_N) experiment, indicating that the weak large-scale uplift movement accounts for the decrease of accumulated stratus precipitation. $-dwqdp$ represents the vertical

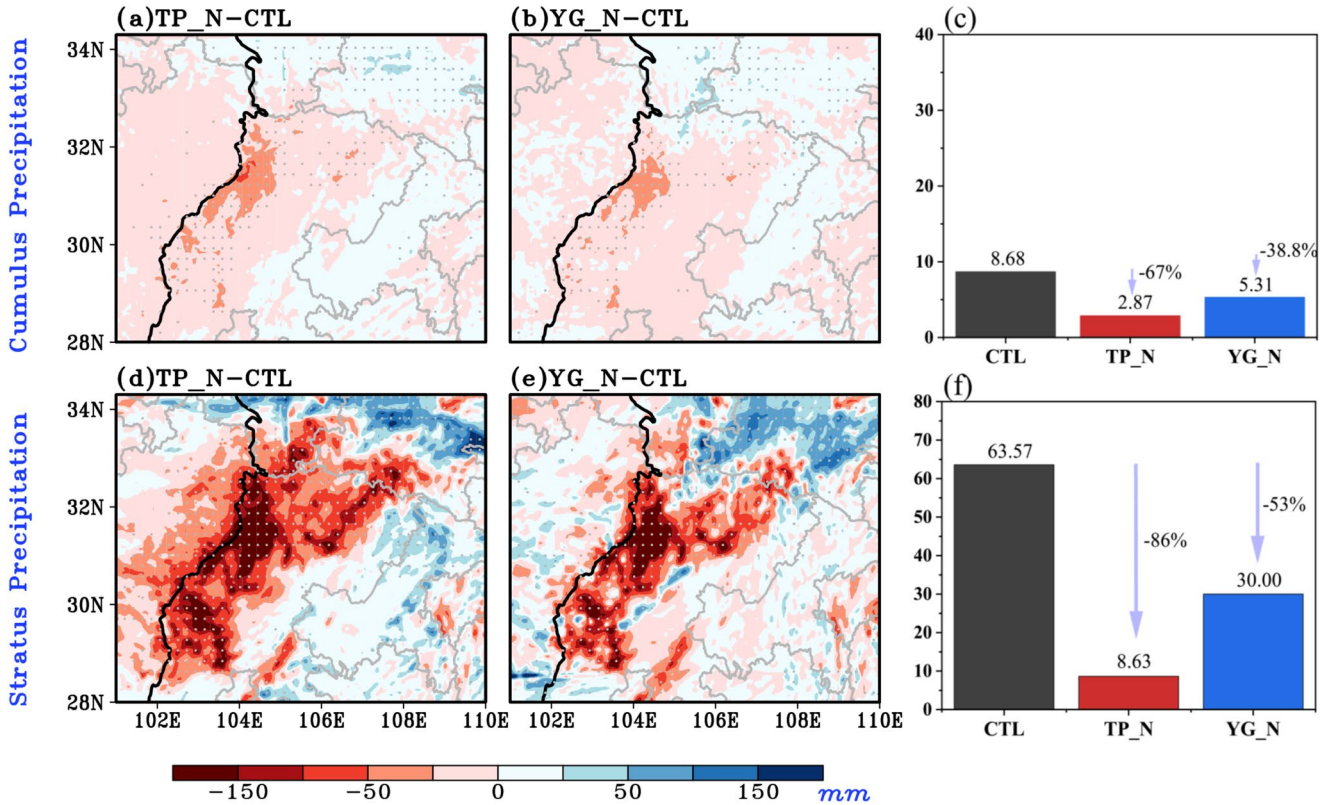

Figure 5. (a and b) The spatial distribution of the difference in the accumulated cumulus and (d–e) stratus precipitation between each sensitive experiment and CTL experiment during 04:00 (BJT) on 11 August-03:00 (BJT) on 13 August 2020. The gray dots symbolize the significance above 95% of the *t*-test. The histogram is the (c) accumulated cumulus and (f) stratus precipitation (unit: mm) during this regional extreme precipitation event regionally averaged over the area of 102°–108°E and 29°–33°N. The number at the top of the bar is a value of regionally averaged rainfall amount. The purple arrows and beside numbers represent the decreased value of rainfall amount relative to the CTL experiment.

transport item, namely the vertical descending or ascending movement of water vapor over the SCB. In the TP_N (YG_N) experiment, the *-dwqdp* is decreased by 1.14 mm·h^{-1} (0.23 mm hr^{-1}) relative to the CTL experiment, implying weakened vertical ascending movement. Besides, the vertical transport item of Equation 1 could be decomposed into three items in Equation 2. Figures 6b and 6d show the thermodynamic, dynamic, and nonlinear items of Equation 2 change with time. It is apparent that the anomalous vertical velocity generated by the changes of atmospheric circulation is the principal factor in the changes of vertical transport items (Figure 6d). E indicates the evaporation rate, which is very small during the REPE (Figure 6a), this is consistent with the findings of Cai et al. (2023). For the account of the balance of the physical equation, the residual term S is large at the hourly scale (Cai et al., 2023; P. Li et al., 2020). In one word, the weakening of both the large-scale thermodynamic ascending motion and the local terrain uplifting effect to airflow is the major cause for the decrease of accumulated total precipitation in the sensitive experiments relative to the CTL experiment.

4.2. The Thermodynamic Process of the Terrain Impact on the REPE

Based on the cognition of moisture budget diagnosis, this section focuses on the thermodynamic process in the weakened large-scale uplift movement using a series of physical quantities. The warm advection can be transported from TP which is as the heat source region relative to the surrounding areas to eastern China in summer (Y. Fu et al., 2020; Ge et al., 2019; G. Wu et al., 2015). When the TP is absent, the thermal contrast between TP and the surrounding regions is weakened and further leads to anomalous cold advection from the TP to the SCB due to the strengthened westerly winds without the blocking of TP. As shown in Figure 7a, compared to the CTL experiment, the enhanced westerly winds due to the absence of TP promote the anomalous cold advection from the upstream region to the SCB in the TP_N experiment. The cold advection that reaches the SCB makes the descending airflow intensify and accumulate in the bottom of the basin. Despite that the cooling is weaker at

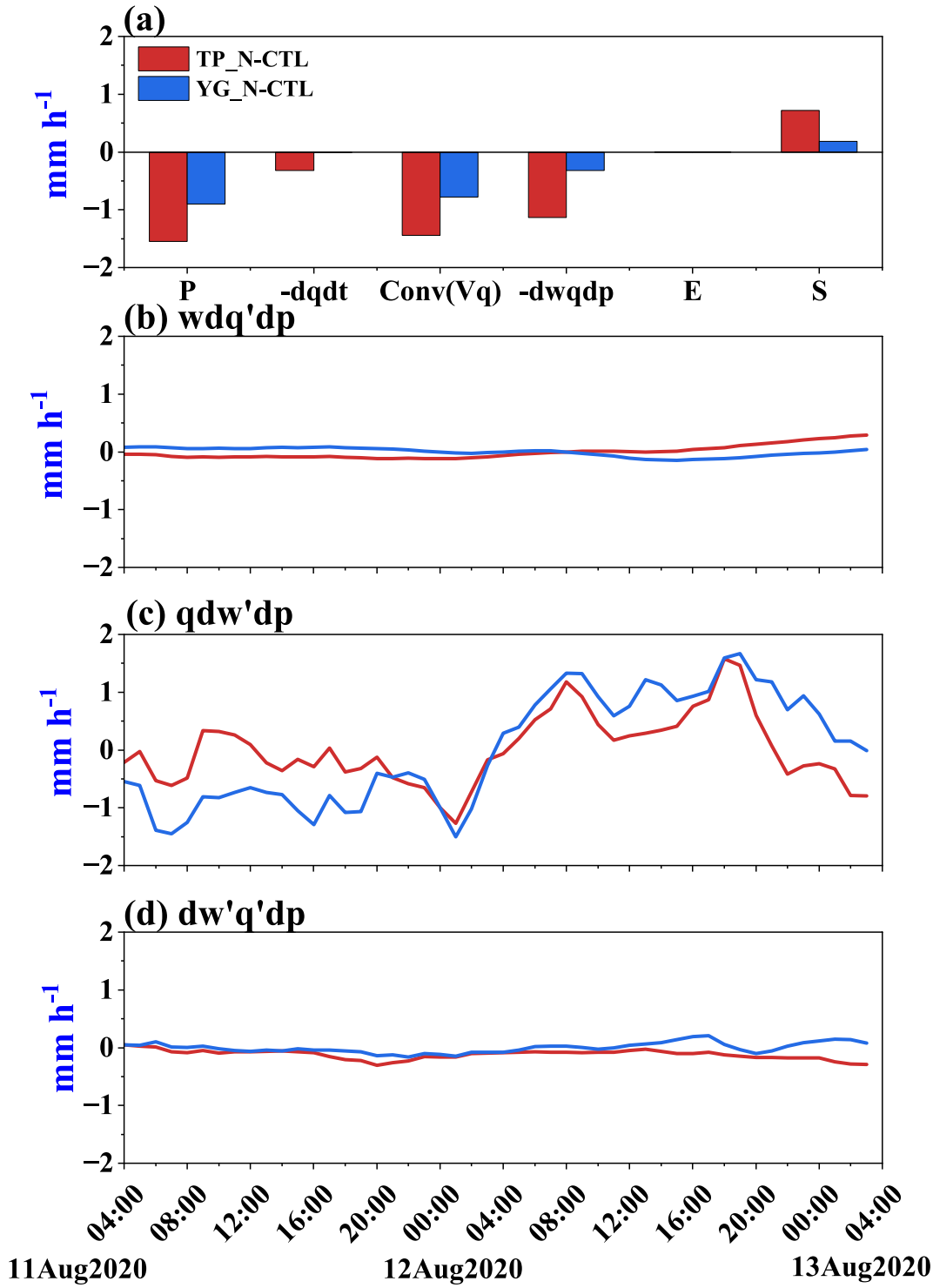

Figure 6. The difference in mean moisture budget components (a) of Equation 1 and the temporal variation of expanded items (b–d) from the vertical item in (a) of Equation 2 during the regional extreme precipitation event regionally averaged over the area of 102°–108°E and 29°–33°N between each sensitive experiment and CTL experiment (unit: mm·h^{-1}).

600 hPa over the east edge of the TP relative to the other regions of SCB, the stronger cooling is in the lower and upper troposphere over the western SCB leading to stable stratification in the TP_N experiment relative to the CTL experiment (Figure 7a). Relative to the CTL experiment, the regional averaged (102°−108°E, 28°–33°N)

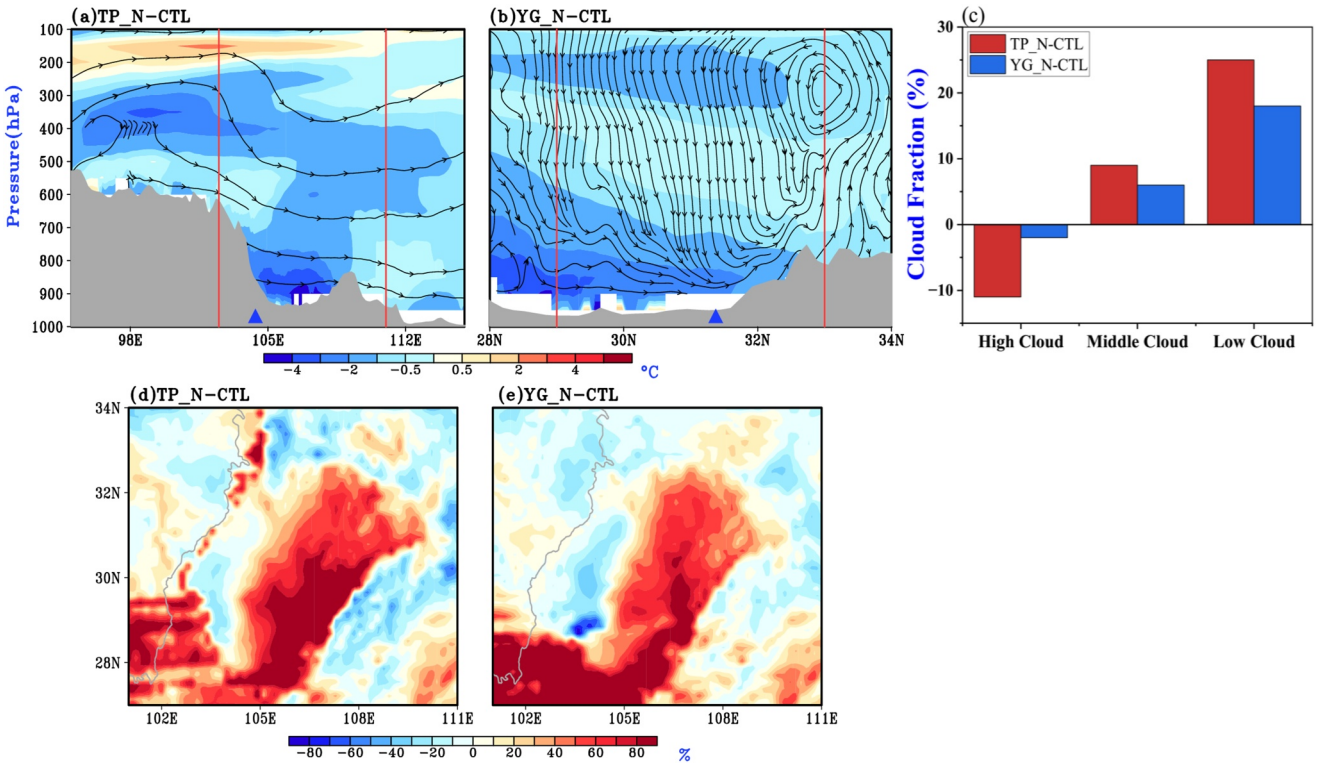

Figure 7. The profile distribution of the difference in mean temperature (shaded, unit: °C) and atmospheric circulation (stream, unit: $m \cdot s^{-1}$) between each sensitive experiment and CTL experiment during 04:00 (BJT) on 11 August to 03:00 (BJT) on 13 August 2020 regionally averaged along 29°–33°N (a) and regionally averaged along 102°–108°E (b). The blue triangle symbolizes the center of difference in accumulated precipitation depicted by Figures 4d and 4e. The area ranged by the red line represents the Sichuan Basin, and the gray shade depicts the terrain profile. The blank portion represents the default value due to the terrain. (c) The histogram of the difference in mean high, middle, and low cloud fractions (unit: %) regionally averaged over the area of 101°–108°E and 26°–34°N during this regional extreme precipitation event (REPE). (d–e) The spatial distribution of the difference in mean middle and low cloud fractions (shaded, unit: %) between each sensitive experiment and CTL experiment during this REPE.

middle and low cloud fractions over the SCB are further increased due to the large-scale anomalous cold advection in the TP_N experiment, which can lead to the negative feedback for temperature in lower troposphere (Figures 7a and 7c). The reduced temperature (Figure 7a) is well corresponding to the increased middle and low cloud fractions (Figure 7d) over most areas of SCB in the TP_N experiment, this is related to the reduced net radiation due to more middle and low clouds (not shown).

In the YG_N experiment, the enhanced southerly winds due to the absence of YGP induce the cold advection from YGP to the SCB relative to the CTL experiment (Figure 7b). Although the thermal contrast between YGP and SCB is much weaker than that between the TP and SCB, the absence of YGP also induces anomalous cold advection from YGP to SCB in the lower troposphere, leading to much more middle and low clouds over eastern SCB in the YG_N experiment relative to the CTL experiment (Figures 7c and 7e), and further promotes in reduced temperature (Figure 2b) due to the negative feedback of clouds, which is similar to the situations when the TP is absent.

The specific humidity differences of −1 to −2.5 $g \cdot kg^{-1}$ and the equivalent potential temperature differences of −4 to 1 K between the TP_N and CTL experiment are located over the western SCB and along the east edge of TP (Figure 8a), corresponding with the atmospheric precipitable water differences of ∼−20 mm over the western SCB (Figure 8c). Relative to the CTL experiment, due to the absence of TP, the largely reduced precipitable water over the western SCB and much more stable large-scale stratification induced by the reduction of the equivalent potential temperature decreasing with altitude over the SCB (Figure 8a) further weaken the large-scale ascending movement (Figures 6a and 7a) and thereafter decrease the stratus rainfall over the western SCB (Figures 4d, 5a, and 5d).

Similar situations can be found when the YGP is absent, the specific humidity differences of ∼−1$g \cdot kg^{-1}$ and the equivalent potential temperature differences of −7 to −2 K between the YG_N and CTL experiment are located over the western SCB (Figure 8b), which imply the more stable large-scale stratification over SCB.

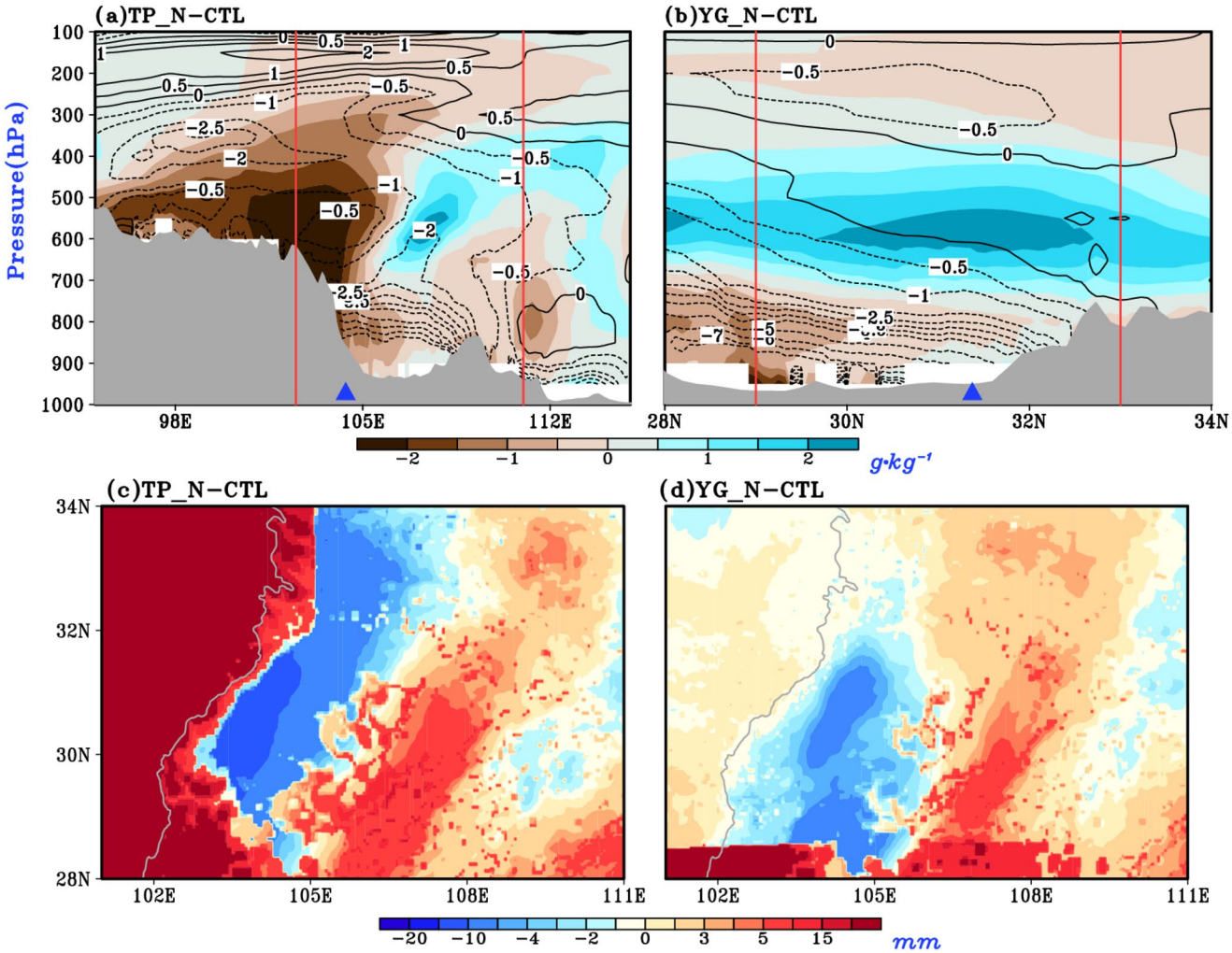

Figure 8. The profile distribution of the difference in mean specific humidity (shaded, unit: g·kg^{-1}) and equivalent potential temperature (contour, unit: K) between each sensitive experiment and CTL experiment during 04:00 (BJT) on 11 August to 03:00 (BJT) on 13 August 2020 regionally averaged along 29°–33°N (a) and 102°–108°E (b). The blue triangle symbolizes the center of difference in accumulated precipitation depicted by Figures 4d and 4e. The areas ranged by the red lines represent the location of Sichuan Basin, and the gray shadings depict the terrain profile. The blank portion represents the default value due to the terrain. (c–d) The distribution of the difference in mean integrated atmospheric precipitable water (shaded, unit: mm) between each sensitive experiment and CTL experiment during this regional extreme precipitation event.

Thereafter, the reduced precipitable water in the YG_N experiment relative to the CTL experiment over the western SCB finally results in less accumulated precipitation over the western SCB (Figure 8d). It is noticed that though the greatly increased atmospheric precipitable water over the east and west of the rainfall center between the sensitive experiment and CTL experiment, but the cold advection, descending air, and decreased equivalent potential temperature result in the stable stratification and thereafter the rainfall is slightly changed over those regions.

In general, due to the absence of TP or YGP, the weakened thermal contrast between the plateau and SCB leads to much more stable large-scale stratification over the SCB, which together with the reduced atmospheric precipitable water over the western SCB further weakens the rainfall during the REPE. Meanwhile, the thermal contrast between the plateau and SCB in the YG_N experiment is weaker than that in TP_N experiment, which is a one of the causes leading to more precipitation in YG_N experiment than that in TP_N experiment.

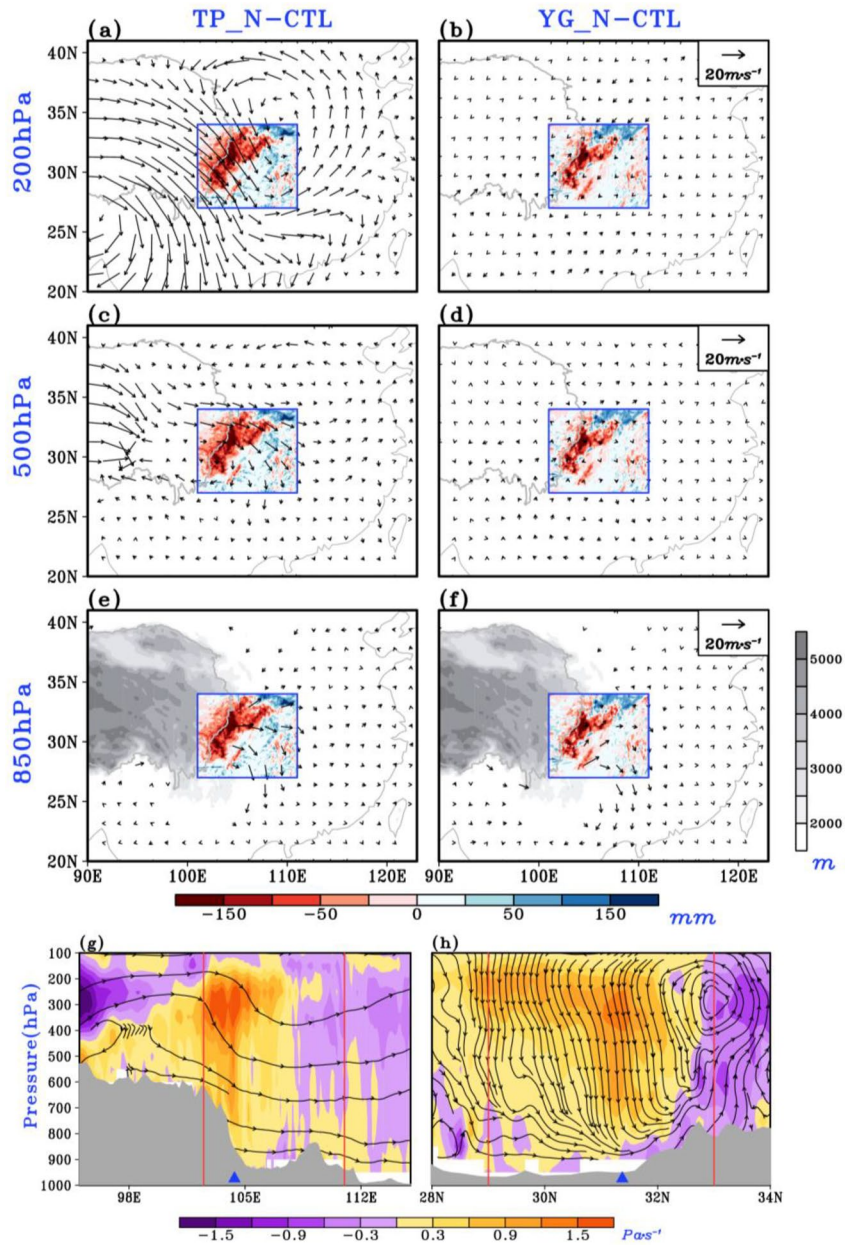

Figure 9. The spatial distribution of the difference in mean wind (vector, unit: m·s^{-1}) at the (a and b) 200 hPa, (c and d) 500 hPa, (e and f) 850 hPa levels and accumulated precipitation (shaded, unit: mm) during 04:00 (BJT) on 11 August-03:00 (BJT) on 13 August 2020 between each sensitive experiment and CTL experiment. The blue rectangles represent the location of Sichuan Basin (SCB). The gray shadings depict the terrain. The profile distribution of the difference in mean vertical velocity (shaded, unit: Pa·s^{-1}) and mean atmospheric circulation (stream, unit: m·s^{-1}) during this regional extreme precipitation event regionally averaged along (g) 29°–33°N and (h) 102°–108°E. The blue triangles symbolize the center of difference in accumulated precipitation depicted by Figures 4d and 4e. The areas ranged by the red line represent the location of SCB, and the gray shade depicts the terrain profile. The blank portion represents the default value due to the terrain.

4.3. The Dynamical Process of the Terrain Impact on REPE

Under a specific atmospheric circulation background, TP and YGP are important for the initiation of synoptic systems in extreme precipitation and the water vapor transport over the SCB (C. H. Huang et al., 2022; Nie & Sun, 2021; H. Xu et al., 2020; Q. Zhang et al., 2017). In this section, we focus on the dynamical process related to the impact of TP or YGP on the vertical velocity during the REPE.

Compared to the CTL experiment, the absence of TP in the TP_N experiment strengthens the westerly winds at 500 and 200 hPa and induces an anomalous cyclone over the area northeast to the SCB and an anomalous anti-cyclone over the areas southwest to the SCB at 200 hPa (Figures 9a and 9c). Meanwhile, an anomalous anti-cyclone at 850 hPa over the SCB can be noted between the TP_N experiment and CTL experiment (Figure 9e), it is well corresponding to the relatively more largely weakened ascending motion over the western SCB and the east edge of TP in the TP_N experiment. Meanwhile, there is an apparent anomalous descending airflow over the rainfall center in the TP_N relative to the CTL experiment, the absence of TP induces the largely weakens the topographic uplift effect to airflow (Figure 9g). Due to the anomalous anti-cyclone at 850 hPa in the TP_N experiment compared to the CTL experiment, the water vapor transport of the western SCB is obviously reduced, resulting in the decrease of accumulated precipitation over the western SCB in the TP_N experiment.

In the YG_N experiment, though the absence of YGP finitely influenced the atmospheric circulation at the 500 and 200 hPa (Figures 9b and 9d). Compared to the CTL experiment, an apparent anomalous anti-cyclone at 850 hPa produced by the YG_N experiment is located over the SCB (Figure 9f). Similarly, owing to the absence of YGP, the uplift effect of terrain on the airflow along the windward over western SCB and north of YGP is restrained in the YG_N experiment (Figure 9h). Similar situations are found in the TP_N experiment, but the less water vapor transport and weaker ascending movement over the western SCB lead to the decrease of precipitation relative to the YG_N experiment. In addition, the water vapor is mainly transported by the southwesterly and southerly winds during this case, the absence of YGP in the YG_N experiment makes more water vapor transport reach SCB than that due to the absence of TP in the TP_N experiment, which accounts for more accumulated precipitation over northern SCB (104°−109°E, 32°–34°N) in the YG_P experiment than that in the TP_N experiment (Figures 4b and 4c).

Overall, relative to the CTL experiment, in the sensitive experiments, the absence of TP or YGP can produce an anomalous anti-cyclone at 850 hPa over the SCB, leading to weakened both the local terrain uplifting effect of airflow along the windward slope and the water vapor transport to the western SCB and thereafter reduced rainfall during the REPE.

5. Conclusion and Discussion

In this study, the impact of the TP or YGP on a REPE in the SCB which occurred during 04:00 BJT on 11 August to 03:00 BJT on 13 August 2020 has been investigated based on numerical experiments. Main findings are shown as follows:

The absence of TP (YGP) can lead to 84% (51%) reduction of accumulated total precipitation over the western SCB during the REPE. And the reduced accumulated total precipitation is mainly caused by the decrease of accumulated stratus precipitation, which can be reduced by 86% (67%) when the TP (YGP) is absent. From the perspective of the thermal process, due to the absence of TP or YGP, large-scale anomalous cold advection from the upstream regions where the terrains are removed leads to reduced temperature over the SCB, and further results in much more stable stratification and less atmospheric precipitable water compared to the CTL experiment and thereafter weakens the ascending motions and reduces the stratus precipitation over the western SCB. From the perspective of the dynamical process, the absence of TP or YGP induces an anomalous anti-cyclone at 850 hPa over the SCB, which further leads to weakened uplifting effect of local terrain on airflow along the windward slope and reduced water vapor transport to the western SCB and thereafter reduces the precipitation over this region (Figure 10).

The quantitative discussion of the topography effect on a REPE provides theoretical support for refined forecasts of extreme precipitation. However, completely separating the dynamical and thermal effects of topography is indeed a difficult thing under the existing experimental design. A common method of dividing these two processes is turning off the surface sensible heat flux change (Z. Q. Wang et al., 2016; Zhao, 2012). We will further investigate the physical mechanism of topographic effect based on more numerical sensitive experiments. On the other hand, the previous studies revealed the quantitative influence of terrain in single extreme precipitation event (Almazroui et al., 2018; Z. Wu et al., 2022; Xia et al., 2021). However, the results based on the single case lack universality. In the future, we need to select more cases and further quantificationally discuss the topographic effect in the thermodynamic and dynamic processes for extreme precipitation under specific atmospheric circulation background on climatic scale.

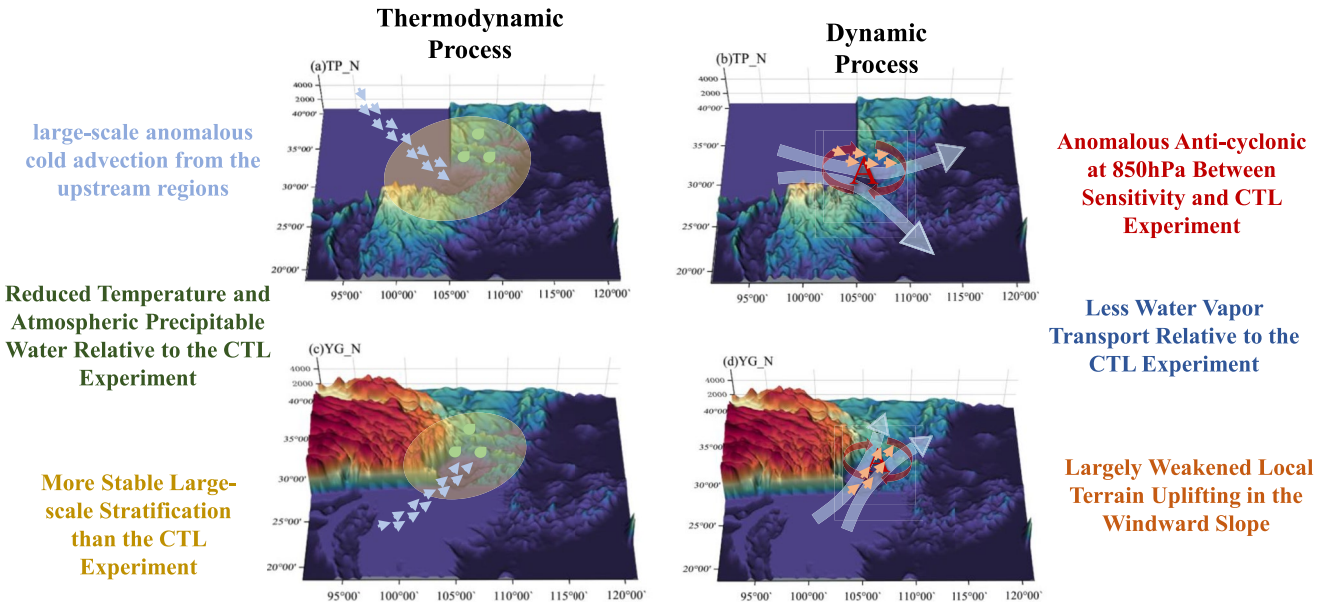

Figure 10. Schematic diagram of the physical mechanisms of the impact of Tibetan Plateau and YGP on this regional extreme precipitation event over Sichuan Basin. The color of the elements in the figure corresponds to the color of the text.

Data Availability Statement

The data used in this study are listed as follows: (a) the GPM-IMERG precipitation data with a horizontal resolution 0.1° (Hou et al., 2014), (b) the ERA5 reanalysis data with a horizontal resolution 0.25° (Hersbach et al., 2020), (c) the National Centers for Environmental Prediction final (FNL) global analysis data with a horizontal resolution 2.5° (National Centers for Environmental Prediction/National Weather Service/NOAA/U.S, 2000), and (d) the numerical model (WRF) used in this study is version 4.2 (Skamarock et al., 2019).

Acknowledgments

This study is funded by the National Natural Science Foundation of China under Grants U2342207 and 42375157, the Open Grants of the State Key Laboratory of Severe Weather (2021LASW-A12), the CAS "Light of West China" Program (E129030101), the Research Funds for the Frontiers Science Center for Critical Earth Material Cycling Nanjing University, the Fundamental Research Funds for the Central Universities (020914380103, 020914380104), the Jiangsu University "Blue Project" outstanding young teachers training object, and the Jiangsu Collaborative Innovation Center for Climate Change. We appreciate the High Performance Computing Center of Nanjing University and the National Key Scientific and Technological Infrastructure project "Earth System Numerical Simulation Facility" (EarthLab) for providing us the computing resource.

References

Almazroui, M., Raju, P. V. S., Yusef, A., Hussein, M. A. A., & Omar, M. (2018). Simulation of an extreme rainfall event of November 2009 over Jeddah, Saudi Arabia: The explicit role of topography and surface heating. *Theoretical and Applied Climatology*, *132*(1–2), 89–101. https://doi.org/10.1007/s00704-017-2080-2

Bao, X., Zhang, F., & Sun, J. (2011). Diurnal variations of warm-season precipitation east of the Tibetan Plateau over China. *Monthly Weather Review*, *139*(9), 2790–2810. https://doi.org/10.1175/MWR-D-11-00006.1

Bin, C., & Xiang, D. X. (2016). Spatiotemporal structure of the moisture sources feeding heavy precipitation events over the Sichuan Basin. *International Journal of Climatology*, *36*(10), 3446–3457. https://doi.org/10.1002/joc.4567

Cai, S., Huang, A., Zhu, K., Guo, W., Wu, Y., & Gu, C. (2023). The forecast skill of the summer precipitation over Tibetan Plateau improved by the adoption of a 3D sub-grid terrain solar radiative effect scheme in a convection-permitting model. *Journal of Geophysical Research: Atmospheres*, *128*(11), e2022JD038105. https://doi.org/10.1029/2022JD038105

Cai, S., Huang, A., Zhu, K., Yang, B., Yang, X., Wu, Y., & Mu, X. (2021). Diurnal cycle of summer precipitation over the Eastern Tibetan Plateau and surrounding regions simulated in a convection-permitting model. *Climate Dynamics*, *57*(1–2), 611–632. https://doi.org/10.1007/s00382-021-05729-5

Cannon, F., Carvalho, L. M., Jones, C., Norris, J., Bookhagen, B., & Kiladis, G. N. (2017). Effects of topographic smoothing on the simulation of winter precipitation in High Mountain Asia. *Journal of Geophysical Research: Atmospheres*, *122*(3), 1456–1474. https://doi.org/10.1002/2016JD026038

Chen, J., Li, C., & He, G. (2007). A diagnostic analysis of the impact of complex terrain in the eastern Tibetan Plateau, China, on a severe storm. *Arctic Antarctic and Alpine Research*, *39*(4), 699–707. https://doi.org/10.1657/1523-0430%2807-500%29%5BCHEN%5D2.0.CO%3B2

Chen, S., Yan, Y., Liu, G., Fang, D., Wu, Z., He, J., & Tang, J. (2019). Spatiotemporal characteristics of precipitation diurnal variations in Chongqing with complex terrain. *Theoretical and Applied Climatology*, *137*(1–2), 1217–1231. https://doi.org/10.1007/s00704-018-2662-7

Chu, Q., Xu, Z., Chen, Y., & Han, D. (2018). Evaluation of the ability of the Weather Research and Forecasting model to reproduce a sub-daily extreme rainfall event in Beijing, China using different domain configurations and spin-up times. *Hydrology and Earth System Sciences*, *22*(6), 3391–3407. https://doi.org/10.5194/hess-22-3391-2018

Collins, W. D., Rasch, P. J., Boville, B. A., Hack, J. J., McCaa, J. R., Williamson, D. L., et al. (2014). Description of the NCAR community atmosphere model (CAM 3.0). *NCAR Technical Note NCAR/TN-464+ STR* (Vol. *226*, pp. 1326–1334).

Cui, T., Li, C., & Tian, F. (2021). Evaluation of temperature and precipitation simulations in CMIP6 models over the Tibetan Plateau. *Earth and Space Science*, *8*(7), e2020EA001620. https://doi.org/10.1029/2020ea001620

Deng, M., Lu, R., & Li, C. (2022). Contrasts between the interannual variations of extreme rainfall over western and eastern Sichuan in mid-summer. *Advances in Atmospheric Sciences*, *1*(6), 999–1011. https://doi.org/10.1007/s00376-021-1219-3

Du, Y., Xu, T., Che, Y., Yang, B., Chen, S., Su, Z., et al. (2022). Uncertainty quantification of WRF model for rainfall prediction over the Sichuan Basin, China. *Atmosphere*, *13*(5), 838. https://doi.org/10.3390/atmos13050838

Formetta, G., Marra, F., Dallan, E., Zaramella, M., & Borga, M. (2022). Differential orographic impact on sub-hourly, hourly, and daily extreme precipitation. *Advances in Water Resources*, *159*, 104085. https://doi.org/10.1016/j.advwatres.2021.104085

Fu, S. M., Mai, Z., Sun, J. H., Li, W. L., Ding, Y., & Wang, Y. Q. (2019). Impacts of convective activity over the Tibetan Plateau on plateau vortex, southwest vortex, and downstream precipitation. *Journal of the Atmospheric Sciences*, *76*(12), 3803–3830. https://doi.org/10.1175/JAS-D-18-0331.1

Fu, Y., Ma, Y., Zhong, L., Yang, Y., Guo, X., Wang, C., et al. (2020). Land-surface processes and summer-cloud-precipitation characteristics in the Tibetan Plateau and their effects on downstream weather: A review and perspective. *National Science Review*, *7*(3), 500–515. https://doi.org/10.1093/nsr/nwz226

Ge, J., You, Q., & Zhang, Y. (2019). Effect of Tibetan Plateau heating on summer extreme precipitation in eastern China. *Atmospheric Research*, *218*, 364–371. https://doi.org/10.1016/j.atmosres.2018.12.018

Grell, G. A., & Freitas, S. R. (2014). A scale and aerosol aware stochastic convective parameterization for weather and air quality modeling. *Atmospheric Chemistry and Physics*, *14*(10), 5233–5250. https://doi.org/10.5194/acp-14-5233-2014

Gu, H., Yu, Z., Peltier, W. R., & Wang, X. (2020). Sensitivity studies and comprehensive evaluation of RegCM4. 6.1 high-resolution climate simulations over the Tibetan Plateau. *Climate Dynamics*, *54*(7–8), 3781–3801. https://doi.org/10.1007/s00382-020-05205-6

Guo, Y., Du, Y., Lu, R., Feng, X., Li, J., Zhang, Y., & Mai, Z. (2022). The characteristics of mesoscale convective systems generated over the Yunnan–Guizhou Plateau during the warm seasons. *International Journal of Climatology*, *42*(14), 7321–7341. https://doi.org/10.1002/joc.7647

Han, J., Du, H., Wu, Z., & He, H. S. (2019). Changes in extreme precipitation over dry and wet regions of China during 1961-2014. *Journal of Geophysical Research: Atmospheres*, *124*(11), 5847–5859. https://doi.org/10.1029/2018JD029974

He, H., & Zhang, F. (2010). Diurnal variations of warm-season precipitation over northern China. *Monthly Weather Review*, *138*(4), 1017–1025. https://doi.org/10.1175/2010MWR3356.1

Hersbach, H., Bell, B., Berrisford, P., Hirahara, S., Horanyi, A., Munoz-Sabater, J., et al. (2020). The ERA5 global reanalysis [Dataset]. Quarterly Journal of the Royal Meteorological Society, *146*(730), 1999–2049. Retrieved from https://cds.climate.copernicus.eu/cdsapp#!/search?type=dataset

Hong, S. Y., Noh, Y., & Dudhia, J. (2006). A new vertical diffusion package with an explicit treatment of entrainment processes. *Monthly Weather Review*, *134*(9), 2318–2341. https://doi.org/10.1175/MWR3199.1

Hou, A. Y., Kakar, R. K., Neeck, S., Azarbarzin, A. A., Kummerow, C. D., Kojima, M., et al. (2014). The global precipitation measurement mission [Dataset]. Bulletin of the American Meteorological Society, *95*(5), 701–722. Retrieved from https://gpm.nasa.gov/data/directory

Hu, X., Yuan, W., & Yu, R. (2021). The extraordinary rainfall over the Eastern Periphery of the Tibetan Plateau in August 2020. *Advances in Atmospheric Sciences*, *38*(12), 2097–2107. https://doi.org/10.1007/s00376-021-1134-7

Hua, S., Xu, X., & Chen, B. (2020). Influence of multiscale orography on the initiation and maintenance of a precipitating convective system in North China: A case study. *Journal of Geophysical Research: Atmospheres*, *125*(13), e2019JD031731. https://doi.org/10.1029/2019JD031731

Huang, C. H., Li, G. P., Niu, J. L., Chen, B., Chen, G., Guo, Y. S., et al. (2022). Dynamic and thermal structure and topographic impact of the night torrential rainfall in Lushan, Sichuan on August 10, 2020. *Chinese Journal of Atmospheric Sciences*, *46*(4), 989–1001. (in Chinese). https://doi.org/10.3878/j.issn.1006-9895.2205.21205

Huang, D., & Gao, S. (2018). Impact of different reanalysis data on WRF dynamical downscaling over China. *Atmospheric Research*, *200*, 25–35. https://doi.org/10.1016/j.atmosres.2017.09.017

Huang, X., Zhou, Y., & Liu, L. (2020). Occurrence and development of an extreme precipitation event in the Ili Valley, Xinjiang, China and analysis of gravity waves. *Atmosphere*, *11*(7), 752. https://doi.org/10.3390/atmos11070752

Jin, X., Wu, T., & Li, L. (2013). The quasi-stationary feature of nocturnal precipitation in the Sichuan Basin and the role of the Tibetan Plateau. *Climate Dynamics*, *41*(3–4), 977–994. https://doi.org/10.1007/s00382-012-1521-y

Kang, Y., Peng, X., Wang, S., Hu, Y., Shang, K., & Lu, S. (2019). Observational analyses of topographic effects on convective systems in an extreme rainfall event in Northern China. *Atmospheric Research*, *229*, 127–144. https://doi.org/10.1016/j.atmosres.2019.05.024

Kuo, H. C., Leou, T. M., & Williams, R. T. (1999). A study on the high-order Smolarkiewicz methods. *Computers & Fluids*, *28*(6), 779–799. https://doi.org/10.1016/S0045-7930(98)00036-X

Lehmann, E. L. (1992). Introduction to Student (1908) The Probable Error of a Mean. In S. Kotz & N. L. Johnson (Eds.), *Breakthroughs in statistics: Methodology and distribution* (pp. 29–32). Springer New York. https://doi.org/10.1007/978-1-4612-4380-9_3

Lei, M., Li, J., Zhang, L., Deng, C., Li, Y., & He, J. (2022). Inconsistent frequency trends between hourly and daily precipitation during warm season in mainland of China. *Geophysical Research Letters*, *49*(19), e2022GL100277. https://doi.org/10.1029/2022GL100277

Li, J., Li, Y., Zhao, T., Schiemann, R., Muetzelfeldt, M., & Jiang, X. (2021). Northeastward propagation of nocturnal precipitation over the Sichuan Basin. *International Journal of Climatology*, *41*(S1), E2863–E2879. https://doi.org/10.1002/joc.6886

Li, L., Zou, Y., Li, Y., Lin, H., Liu, D. L., Wang, B., et al. (2020). Trends, change points and spatial variability in extreme precipitation events from 1961 to 2017 in China. *Hydrology Research*, *51*(3), 484–504. https://doi.org/10.2166/nh.2020.095

Li, P., Furtado, K., Zhou, T., Chen, H., Li, J., Guo, Z., & Xiao, C. (2020). The diurnal cycle of East Asian summer monsoon precipitation simulated by the Met Office Unified Model at convection permitting scales. *Climate Dynamics*, *55*(1–2), 131–151. https://doi.org/10.1007/s00382-018-4368-z

Li, X., Zhang, K., Bao, H., & Zhang, H. (2022). Climatology and changes in hourly precipitation extremes over China during 1970–2018. *Science of the Total Environment*, *839*, 156297. https://doi.org/10.1016/j.scitotenv.2022.156297

Lin, R., Zhou, T., & Qian, Y. (2014). Evaluation of global monsoon precipitation changes based on five reanalysis datasets. *Journal of Climate*, *27*(3), 1271–1289. https://doi.org/10.1175/JCLI-D-13-00215.1

Liu, J., Yang, L., Jiang, J., Yuan, W., & Duan, Z. (2021). Mapping diurnal cycles of precipitation over China through clustering. *Journal of Hydrology*, *592*, 125804. https://doi.org/10.1016/j.jhydrol.2020.125804

Liu, Y., Lu, M., Yang, H., Duan, A., He, B., Yang, S., & Wu, G. (2020). Land–atmosphere–ocean coupling associated with the Tibetan Plateau and its climate impacts. *National Science Review*, *7*(3), 534–552. https://doi.org/10.1093/nsr/nwaa011

Liu, Y., Zhuo, L., & Han, D. (2023). Developing spin-up time framework for WRF extreme precipitation simulations. *Journal of Hydrology*, *620*, 129443. https://doi.org/10.1016/j.jhydrol.2023.129443

Luo, Y., Wu, M., Ren, F., Li, J., & Wong, W. K. (2016). Synoptic situations of extreme hourly precipitation over China. *Journal of Climate*, *29*(24), 8703–8719. https://doi.org/10.1175/JCLI-D-16-0057.1

Ma, Q. R., Jia, F., Wu, X. X., Chang, Y. Z., Zhi, R., & Feng, G. L. (2022). Characteristics and related mechanisms of the persistent extreme precipitation in August 2020 over Western China. *Frontiers in Earth Science*, *10*, 1004612. https://doi.org/10.3389/feart.2022.1004612

Ma, S., & Zhou, T. (2015). Precipitation changes in wet and dry seasons over the 20th century simulated by two versions of the FGOALS model. *Advances in Atmospheric Sciences*, *32*(6), 839–854. https://doi.org/10.1007/s00376-014-4136-x

Morrison, H., Thompson, G., & Tatarskii, V. (2009). Impact of cloud microphysics on the development of trailing stratiform precipitation in a simulated squall line: Comparison of one– and two–moment schemes. *Monthly Weather Review*, *137*(3), 991–1007. https://doi.org/10.1175/2008MWR2556.1

Mun, J., Lee, H. W., Jeon, W., & Lee, S. H. (2017). Impact of meteorological initial input data on WRF simulation-Comparison of ERA-interim and FNL data. *Journal of Environmental Science International*, *26*(12), 1307–1319. https://doi.org/10.5322/JESI.2017.26.12.1307

National Centers for Environmental Prediction/National Weather Service/NOAA/U.S. Department of Commerce. (2000). NCEP FNL Operational Model Global Tropospheric Analyses, continuing from July 1999 (Updated daily) [Dataset]. Research Data Archive at the National Center for Atmospheric Research, Computational and Information Systems Laboratory. https://doi.org/10.5065/D6M043C6

Ng, C. P., Zhang, Q., & Li, W. (2021). Changes in hourly extreme precipitation over eastern China from 1970 to 2019 dominated by synoptic-scale precipitation. *Geophysical Research Letters*, *48*(5), e2020GL090620. https://doi.org/10.1029/2020GL090620

Nie, Y., & Sun, J. (2021). Synoptic-scale circulation precursors of extreme precipitation events over Southwest China during the rainy season. *Journal of Geophysical Research: Atmospheres*, *126*(13), e2021JD035134. https://doi.org/10.1029/2021JD035134

Nielsen, E. R., Schumacher, R. S., & Keclik, A. M. (2016). The effect of the Balcones Escarpment on three cases of extreme precipitation in central Texas. *Monthly Weather Review*, *144*(1), 119–138. https://doi.org/10.1175/MWR-D-15-0156.1

Park, I. H., & Min, S. K. (2017). Role of convective precipitation in the relationship between subdaily extreme precipitation and temperature. *Journal of Climate*, *30*(23), 9527–9537. https://doi.org/10.1175/jcli-d-17-0075.1

Phadtare, J. (2018). Role of Eastern Ghats orography and cold pool in an extreme rainfall event over Chennai on 1 December 2015. *Monthly Weather Review*, *146*(4), 943–965. https://doi.org/10.1175/MWR-D-16-0473.1

Qian, C., Ye, Y., Zhang, W., & Zhou, T. (2022). Heavy rainfall event in mid-August 2020 in southwestern China: Contribution of anthropogenic forcings and atmospheric circulation. *Bulletin of the American Meteorological Society*, *103*(3), S111–S117. https://doi.org/10.1175/BAMS-D-21-0233.1

Qiao, P., Gong, Z., Liu, W., Zhang, Y., & Feng, G. (2022). Asymmetrical synchronization of extreme rainfall events in southwest China. *International Journal of Climatology*, *42*(11), 5935–5948. https://doi.org/10.1002/joc.7569

Roe, G. H. (2005). Orographic precipitation. *Annual Review of Earth and Planetary Sciences*, *33*(1), 645–671. https://doi.org/10.1146/annurev.earth.33.092203.122541

Seager, R., Naik, N., & Vecchi, G. A. (2010). Thermodynamic and dynamic mechanisms for large-scale changes in the hydrological cycle in response to global warming. *Journal of Climate*, *23*(17), 4651–4668. https://doi.org/10.1175/2010JCLI3655.1

Shen, C., Li, G., & Dong, Y. (2022). Vertical structures associated with orographic precipitation during warm season in the Sichuan Basin and its surrounding areas at different altitudes from 8-year GPM DPR observations. *Remote Sensing*, *14*(17), 4222. https://doi.org/10.3390/rs14174222

Shi, Z., Sha, Y., & Liu, X. (2017). Effect of Yunnan–Guizhou topography at the southeastern Tibetan Plateau on the Indian monsoon. *Journal of Climate*, *30*(4), 1259–1272. https://doi.org/10.1175/JCLI-D-16-0105.1

Short, C. J., & Petch, J. (2022). Reducing the spin-up of a regional NWP system without data assimilation. *Quarterly Journal of the Royal Meteorological Society*, *148*(745), 1623–1643. https://doi.org/10.1002/qj.4268

Skamarock, W. C., Klemp, J. B., Dudhia, J., Gill, D. O., Liu, Z., Berner, J., et al. (2019). A description of the advanced research WRF model version 4 [Software]. National Center for Atmospheric Research, *145*(145), 550. Zenodo. https://doi.org/10.5281/zenodo.10098038

Son, J. H., Seo, K. H., & Wang, B. (2020). How does the Tibetan Plateau dynamically affect downstream monsoon precipitation? *Geophysical Research Letters*, *47*(23), e2020GL090543. https://doi.org/10.1029/2020GL090543

Student. (1908). The probable error of a mean. *Biometrika*, *6*(1), 1–25. https://doi.org/10.2307/2331554

Sun, J., & Zhang, F. (2012). Impacts of mountain–plains solenoid on diurnal variations of rainfalls along the Mei-yu front over the East China Plains. *Monthly Weather Review*, *140*(2), 379–397. https://doi.org/10.1175/MWR-D-11-00041.1

Tang, G., Long, D., Hong, Y., Gao, J., & Wan, W. (2018). Documentation of multifactorial relationships between precipitation and topography of the Tibetan Plateau using spaceborne precipitation radars. *Remote Sensing of Environment*, *208*, 82–96. https://doi.org/10.1016/j.rse.2018.02.007

Tewari, M., Chen, F., Wang, W., Dudhia, J., LeMone, M. A., Mitchell, K., et al. (2004). Implementation and verification of the unified NOAH land surface model in the WRF model. *20th conference on weather analysis and forecasting/16th conference on numerical weather prediction*, *1115*(6), 2165–2170.

Ulmer, F. G., & Balss, U. (2016). Spin-up time research on the weather research and forecasting model for atmospheric delay mitigations of electromagnetic waves. *Journal of Applied Remote Sensing*, *10*(1), 016027. https://doi.org/10.1117/1.JRS.10.016027

Wan, B., Gao, Z., Chen, F., & Lu, C. (2017). Impact of Tibetan Plateau surface heating on persistent extreme precipitation events in southeastern China. *Monthly Weather Review*, *145*(9), 3485–3505. https://doi.org/10.1175/MWR-D-17-0061.1

Wang, Q., Xue, M., & Tan, Z. (2016). Convective initiation by topographically induced convergence forcing over the Dabie Mountains on 24 June 2010. *Advances in Atmospheric Sciences*, *33*(10), 1120–1136. https://doi.org/10.1007/s00376-016-6024-z

Wang, Q. W., & Tan, Z. M. (2014). Multi-scale topographic control of southwest vortex formation in Tibetan Plateau region in an idealized simulation. *Journal of Geophysical Research: Atmospheres*, *119*(20), 11–543. https://doi.org/10.1002/2014JD021898

Wang, Y., Yang, K., Zhou, X., Chen, D., Lu, H., Ouyang, L., et al. (2020). Synergy of orographic drag parameterization and high resolution greatly reduces biases of WRF-simulated precipitation in central Himalaya. *Climate Dynamics*, *54*(3–4), 1729–1740. https://doi.org/10.1007/s00382-019-05080-w

Wang, Z. Q., Duan, A. M., Li, M. S., & He, B. (2016). Influences of thermal forcing over the slope/platform of the Tibetan Plateau on Asian summer monsoon: Numerical studies with the WRF model. *Chinese Journal of Geophysics*, *59*(5), 474–487. https://doi.org/10.1002/cjg2.30007

Wei, W., Zhang, R., Wen, M., Rong, X., & Li, T. (2014). Impact of Indian summer monsoon on the South Asian High and its influence on summer rainfall over China. *Climate Dynamics*, *43*(5), 1257–1269. https://doi.org/10.1007/s00382-013-1938-y

Wu, A., & Li, G. (2022). Roles of the topographically-affected boundary layer low-level jet in the moisture transport process of nocturnal rainstorms in mountainous areas around the western Sichuan Basin. *Atmosphere*, *14*(1), 84. https://doi.org/10.3390/atmos14010084

Wu, G., Duan, A., Liu, Y., Mao, J., Ren, R., Bao, Q., et al. (2015). Tibetan Plateau climate dynamics: Recent research progress and outlook. *National Science Review*, *2*(1), 100–116. https://doi.org/10.1093/nsr/nwu045

Wu, M. G., & Luo, Y. L. (2019). Extreme hourly precipitation over China: Research progress from 2010 to 2019. *Torrential Rain and Disasters*, *38*(5), 502–514.

Wu, Y., Huang, A., Huang, D., Chen, F., Yang, B., Zhou, Y., et al. (2018). Diurnal variations of summer precipitation over the regions east to Tibetan Plateau. *Climate Dynamics*, *51*(11–12), 4287–4307. https://doi.org/10.1007/s00382-017-4042-x

Wu, Z., Liu, H., Chan, K. T., Wu, K., Zhang, W., & Wang, D. (2022). Effects of topography and latent heat on the evolution of a mesoscale dual-core southwest vortex over Sichuan Basin, China. *Frontiers in Earth Science*, *10*, 827601. https://doi.org/10.3389/feart.2022.827601/full

Xia, R., Luo, Y., Zhang, D. L., Li, M., Bao, X., & Sun, J. (2021). On the diurnal cycle of heavy rainfall over the Sichuan Basin during 10–18 August 2020. *Advances in Atmospheric Sciences*, *38*(12), 2183–2200. https://doi.org/10.1007/s00376-021-1118-7

Xu, H., Goldsmith, Y., Lan, J., Tan, L., Wang, X., Zhou, X., et al. (2020). Juxtaposition of western Pacific subtropical high on Asian Summer Monsoon shapes subtropical East Asian precipitation. *Geophysical Research Letters*, *47*(3), e2019GL084705. https://doi.org/10.1029/2019GL084705

Xu, H., & Yao, W. (2015). A numerical study of the Beijing extreme rainfall of 21 July 2012 and the impact of topography. *Advances in Meteorology*, *2015*, 1–12. https://doi.org/10.1155/2015/980747

Xu, W., & Zipser, E. J. (2011). Diurnal variations of precipitation, deep convection, and lightning over and east of the eastern Tibetan Plateau. *Journal of Climate*, *24*(2), 448–465. https://doi.org/10.1175/2010JCLI3719.1

Xu, X., Huang, A., Huang, D., Zhang, Y., Gu, C., Cai, S., et al. (2023). What are the dominant synoptic patterns leading to the summer regional hourly extreme precipitation events over central-eastern Tibetan Plateau and Sichuan Basin? *Geophysical Research Letters*, *50*(5), e2022GL102342. https://doi.org/10.1029/2022GL102342

Yang, K., Chen, J., Lu, C., Li, J., Liu, T., Deng, L., & Li, Y. (2022). Impacts of regional uplift of the Tibetan Plateau on local summer precipitation and downstream moisture budget: A simulation study. *International Journal of Climatology*, *42*(16), 8882–8903. https://doi.org/10.1002/joc.7781

Yang, M., Liu, G., Chen, T., Chen, Y., & Xia, C. (2020). Evaluation of GPM IMERG precipitation products with the point rain gauge records over Sichuan, China. *Atmospheric Research*, *246*, 105101. https://doi.org/10.1016/j.atmosres.2020.105101

Zhang, J., & Sun, X. (2021). Characteristics and cause analysis on a continuous severe rainstorm process in Sichuan Basin from August 10 to 14, 2020 (In Chinese). *Plateau and Mountain Meteorology Research*, *42*(3), 1674–2184. https://doi.org/10.3969/j.issn.1674-2184.2021.03.007

Zhang, Q., Zheng, Y., Singh, V. P., Luo, M., & Xie, Z. (2017). Summer extreme precipitation in eastern China: Mechanisms and impacts. *Journal of Geophysical Research: Atmospheres*, *122*(5), 2766–2778. https://doi.org/10.1002/2016JD025913

Zhang, Y., Sun, J., Zhu, L., Tang, H., Jin, S., & Liu, X. (2021). Comparison of two types of persistent heavy rainfall events during sixteen warm seasons in the Sichuan Basin. *Atmospheric and Oceanic Science Letters*, *14*(6), 100094. https://doi.org/10.1016/j.aosl.2021.100094

Zhang, Y., Xue, M., Zhu, K., & Zhou, B. (2019). What is the main cause of diurnal variation and nocturnal peak of summer precipitation in Sichuan Basin, China? The key role of boundary layer low-level jet inertial oscillations. *Journal of Geophysical Research: Atmospheres*, *124*(5), 2643–2664. https://doi.org/10.1029/2018JD029834

Zhao, Y. (2012). Numerical investigation of a localized extremely heavy rainfall event in complex topographic area during midsummer. *Atmospheric Research*, *113*, 22–39. https://doi.org/10.1016/j.atmosres.2012.04.018

Zhao, Y., Huang, A., Kan, M., Dong, X., Yu, X., Wu, Y., et al. (2020). Characteristics of hourly extreme precipitation along the Yangtze River Basin, China during warm season. *Scientific Reports*, *10*(1), 1–13. https://doi.org/10.1038/s41598-020-62535-5

Zheng, Y., Gong, Y., Chen, J., & Tian, F. (2019). Warm-season diurnal variations of total, stratiform, convective, and extreme hourly precipitation over central and eastern China. *Advances in Atmospheric Sciences*, *36*(2), 143–159. https://doi.org/10.1007/s00376-018-7307-3

Zhu, D., Yang, Q., Xiong, K., & Xiao, H. (2022). Spatiotemporal variations in daytime and night-time precipitation on the Yunnan–Guizhou Plateau from 1960 to 2017. *Atmosphere*, *13*(3), 415. https://doi.org/10.3390/atmos13030415

Zhu, L., Liu, J., Zhu, A. X., Sheng, M., & Duan, Z. (2018). Spatial distribution of diurnal rainfall variation in summer over China. *Journal of Hydrometeorology*, *19*(4), 667–678. https://doi.org/10.1175/JHM-D-17-0176.1